Plasmonic behaviors of metallic AZO thin film and AZO nanodisk array

Jia-Yu Lin, Kun-Da Zhong, and Po-Tsung Lee*

Department of Photonics & Institute of Electro-Optical Engineering, National Chiao Tung University, Room 401 CPT Building, 1001 Ta-Hsueh Road, Hsinchu 300, Taiwan

potsung@mail.nctu.edu.tw

Abstract: Aluminum-doped zinc oxide (AZO) is well known as transparent conducting material for electro-optical devices, but is rarely used as plasmonic material, particularly on the localized surface plasmon resonance (LSPR) behavior of AZO nanostructure and its plasmonic devices. In this study, we systematically investigate the plasmonic behaviors of AZO thin films and patterned AZO nanostructures with various structural dimensions under different annealing treatments. We find that AZO film can possess highly-tunable, metal-like, and low-loss plasmonic property and the LSPR characteristic of AZO nanostructure is observed in the near-infrared (NIR) region under proper annealing conditions. Finally, environmental index sensing is performed to demonstrate the capability of AZO nanostructure for optical sensing application. High index sensitivity of 873 nm per refractive index unit (RIU) variation is obtained in experiment.

OCIS codes: (240.6680) Surface plasmons; (250.5403) Plasmonics; (280.4788) Optical sensing and sensors; (310.6628) Subwavelength structures, nanostructures; (310.6860) Thin films, optical properties.

References and links

1. D. K. Gramotnev and S. I. Bozhevolnyi, "Plasmonics beyond the diffraction limit," Nat. Photonics **5**(2), 83–91 (2010).
2. J. A. Schuller, E. S. Barnard, W. Cai, Y. C. Jun, J. S. White, and M. L. Brongersma, "Plasmonics for extreme light concentration and manipulation," Nat. Mater. **9**(3), 193–204 (2010).
3. S. Ishii, M. Y. Shalaginov, V. E. Babicheva, A. Boltasseva, and A. V. Kildishev, "Plasmonic waveguides cladded by hyperbolic metamaterials," Opt. Lett. **39**(16), 4663–4666 (2014).
4. H. A. Atwater and A. Polman, "Plasmonics for improved photovoltaic devices," Nat. Mater. **9**(3), 205–213 (2010).
5. C. D'Andrea, J. Bochterle, A. Toma, C. Huck, F. Neubrech, E. Messina, B. Fazio, O. M. Maragò, E. Di Fabrizio, M. Lamy de La Chapelle, P. G. Gucciardi, and A. Pucci, "Optical nanoantennas for multiband surface-enhanced infrared and Raman spectroscopy," ACS Nano **7**(4), 3522–3531 (2013).
6. R. Ahijado-Guzmán, J. Prasad, C. Rosman, A. Henkel, L. Tome, D. Schneider, G. Rivas, and C. Sönnichsen, "Plasmonic nanosensors for simultaneous quantification of multiple protein-protein binding affinities," Nano Lett. **14**(10), 5528–5532 (2014).
7. M. L. Juan, M. Righini, and R. Quidant, "Plasmon nano-optical tweezers," Nat. Photonics **5**(6), 349–356 (2011).
8. T. Ergin, N. Stenger, P. Brenner, J. B. Pendry, and M. Wegener, "Three-dimensional invisibility cloak at optical wavelengths," Science **328**(5976), 337–339 (2010).
9. Z. Jacob, L. V. Alekseyev, and E. Narimanov, "Optical hyperlens: far-field imaging beyond the diffraction limit," Opt. Express **14**(18), 8247–8256 (2006).
10. P. A. Huidobro, M. L. Nesterov, L. Martín-Moreno, and F. J. García-Vidal, "Transformation optics for plasmonics," Nano Lett. **10**(6), 1985–1990 (2010).
11. R. Maas, J. Parsons, N. Engheta, and A. Polman, "Experimental realization of an epsilon-near-zero metamaterial at visible wavelengths," Nat. Photonics **7**(11), 907–912 (2013).
12. G. V. Naik, A. Boltasseva, "A comparative study of semiconductor-based plasmonic metamaterials," Metamaterials (Amst.) **5**(1), 1–7 (2011).
13. G. V. Naik, V. M. Shalaev, and A. Boltasseva, "Alternative plasmonic materials: beyond gold and silver," Adv. Mater. **25**(24), 3264–3294 (2013).
14. M. Nezhad, K. Tetz, and Y. Fainman, "Gain assisted propagation of surface plasmon polaritons on planar metallic waveguides," Opt. Express **12**(17), 4072–4079 (2004).

#255390 Received 10 Dec 2015; revised 17 Feb 2016; accepted 25 Feb 2016; published 1 Mar 2016

15. P. R. West, S. Ishii, G. V. Naik, N. K. Emani, V. M. Shalaev, and A. Boltasseva, "Searching for better plasmonic materials," Laser Photonics Rev. **4**(6), 795–808 (2010).
16. H. Saarenpää, T. Niemi, A. Tukiainen, H. Lemmetyinen, and N. Tkachenko, "Aluminum doped zinc oxide films grown by atomic layer deposition for organic photovoltaic devices," Sol. Energy Mater. Sol. Cells **94**(8), 1379–1383 (2010).
17. M. Sessolo and H. J. Bolink, "Hybrid organic-inorganic light-emitting diodes," Adv. Mater. **23**(16), 1829–1845 (2011).
18. W. Gao and Z. W. Li, "Photoluminescence properties of ZnO films grown by wet oxidation: effect of processing," J. Alloys Compd. **449**(1–2), 202–206 (2008).
19. E. E. Khawaja, S. M. A. Durrani, and A. M. Al-Shukri, "Simple method for determining the optical constants of thin metallic films from transmittance measurements," Thin Solid Films **358**(1–2), 166–171 (2000).
20. F. Lai, L. Lin, R. Gai, Y. Lin, and Z. Huang, "Determination of optical constants and thicknesses of In_2O_3:Sn films from transmittance data," Thin Solid Films **515**(18), 7387–7392 (2007).
21. A. Janotti and C. G. Van de Walle, "Fundamentals of zinc oxide as a semiconductor," Rep. Prog. Phys. **72**(12), 126501 (2009).
22. Y. Kim, W. Lee, D.-R. Jung, J. Kim, S. Nam, H. Kim, and B. Park, "Optical and electronic properties of post-annealed ZnO:Al thin films," Appl. Phys. Lett. **96**(17), 171902 (2010).
23. X. T. Zhang, Y. C. Liu, Z. Z. Zhi, J. Y. Zhang, Y. M. Lu, D. Z. Shen, W. Xu, G. Z. Zhong, X. W. Fan, and X. G. Kong, "Resonant Raman scattering and photoluminescence from high-quality nanocrystalline ZnO thin films prepared by thermal oxidation of ZnS thin films," J. Phys. D Appl. Phys. **34**(24), 3430–3433 (2001).
24. H. Tong, Z. Deng, Z. Liu, C. Huang, J. Huang, H. Lan, C. Wang, and Y. Cao, "Effects of post-annealing on structural, optical and electrical properties of Al-doped ZnO thin films," Appl. Surf. Sci. **257**(11), 4906–4911 (2011).
25. M. K. Puchert, P. Y. Timbrell, and R. N. Lamb, "Postdeposition annealing of radio frequency magnetron sputtered ZnO films," J. Vac. Sci. Technol. A **14**(4), 2220–2230 (1996).
26. A. L. Patterson, "The Scherrer formula for X-Ray particle size determination," Phys. Rev. **56**(10), 978–982 (1939).
27. J. Tauc, "Absorption edge and internal electric fields in amorphous semiconductors," Mater. Res. Bull. **5**(8), 721–729 (1970).
28. E. Burstein, "Anomalous optical absorption limit in InSb," Phys. Rev. **93**(3), 632–633 (1954).
29. W. Yang, Z. Wu, Z. Liu, A. Pang, Y.-L. Tu, and Z. C. Feng, "Room temperature deposition of Al-doped ZnO films on quartz substrates by radio-frequency magnetron sputtering and effects of thermal annealing," Thin Solid Films **519**(1), 31–36 (2010).
30. P. B. Johnson and R. W. Christy, "Optical constants of the noble metals," Phys. Rev. B **6**(12), 4370–4379 (1972).
31. J. Zuloaga and P. Nordlander, "On the energy shift between near-field and far-field peak intensities in localized plasmon systems," Nano Lett. **11**(3), 1280–1283 (2011).
32. J. Aizpurua, G. W. Bryant, L. J. Richter, F. J. García de Abajo, B. K. Kelley, and T. Mallouk, "Optical properties of coupled metallic nanorods for field-enhanced spectroscopy," Phys. Rev. B **71**(23), 235420 (2005).
33. J. Ye, C. Chen, W. V. Roy, P. V. Dorpe, G. Maes, and G. Borghs, "The fabrication and optical property of silver nanoplates with different thicknesses," Nanotechnology **19**(32), 325702 (2008).

1. Introduction

Plasmonics is a subfield of nanophotonics and has received much attention in the last decade because it provides the way to manipulate light at the nanoscale beyond the optical diffraction limit [1,2]. Surface plasmon resonances (SPRs) are the collective oscillation of free electrons excited by incident light at specific frequency on the metal surface. In metallic nanostructures, the light field can be localized at subwavelength scale and enhanced by several orders of magnitude when localized surface plasmon resonance (LSPR) occurs. The optical properties of the localized and enhanced field at metal surface have been extensively applied to various applications, such as subwavelength waveguides [3], light concentrators [4], surface enhanced infrared absorption [5], biochemical nano-sensors [6], and optical tweezers [7]. Furthermore, combining plasmonics and metamaterials facilitates the development of novel devices with the unprecedented functionalities like optical invisibility cloaks [8], hyperlenses [9], transformation optics [10], and epsilon-near-zero [11]. Generally, plasmonic devices are made from metal materials (e.g. silver or gold) due to the fact that metals have abundant free electrons to provide negative real permittivity. However, metals suffer from large losses including carrier scattering damping and carrier transitions in optical frequencies [12,13]. The losses are detrimental to the performance of plasmonic devices and seriously limit the feasibility of plasmonic application [14]. In fact, transparent conducting oxide (TCO), such as

#255390 Received 10 Dec 2015; revised 17 Feb 2016; accepted 25 Feb 2016; published 1 Mar 2016

aluminum-doped zinc oxide (AZO), could be a suitable candidate as plasmonic materials in the near-infrared (NIR) region [15]. By controlling the deposition and annealing conditions, the carrier concentration can be easily tuned to obtain high doping level ($>10^{20}$ cm^{-3}) owing to large solid-solubilities for dopants. In addition, TCO with large bandgap experiences little interband transition loss in the NIR region. Thus, TCO can be regarded as low-loss plasmonic material in the NIR region.

Although TCO is well known as transparent conducting material for electro-optical devices, such as solar cells [16] and light emitting diodes [17] for a long time, it is rarely explored as plasmonic material, particularly on the LSPR behaviors of TCO nanostructure and its corresponding plasmonic devices. Among various TCOs, AZO is especially attractive for optoelectronic devices due to the advantages of relatively cheap, abundant elements, good thermal stability, non-toxicity, and stability in hydrogen plasmon processes. In addition, AZO film possesses high *c*-axis orientated crystalline structure (002) that can improve the carrier mobility by reducing the probability of the scattering of charge carriers at grain boundary, thereby leading to lower ohmic loss [18]. In this study, AZO films under various processing conditions are grown by radio-frequency (RF) magnetron sputtering system to investigate their metallic properties through the electric, optical, and structural analysis. Furthermore, the patterned AZO nanostructures with various structural dimensions under different annealing treatments are fabricated and simulated to examine their LSPR behaviors. To avoid complexity, simple nanodisk structures are employed to analyze their optical characteristics. It is found that the optical properties of the metallic AZO nanostructures are very similar to those of the conventional metal ones. In other words, it is promising that plasmonic devices with high performance can be achieved by replacing metals with low-loss AZO material in the NIR region. Finally, environmental index sensing is performed to evaluate the capacity of plasmonic nano-sensor using metallic AZO material.

2. Methods

A series of AZO films deposited on quartz substrates are prepared by RF magnetron sputtering system at room temperature and annealed for structural, electric, and optical analysis. A sintered ceramic sputter target with a mixture of ZnO and Al_2O_3 (2 wt. %) is used as source material. The working pressure, Ar flow rate, and RF power are set as 2 mTorr, 30 sccm, and 45 W. The dielectric functions of AZO films are retrieved by fitting the experimental and theoretical transmittance curves in the range from 1500 nm to 4000 nm according to Drude-Lorentz model, and similar fitting methods have been reported in other literatures [19,20]. The calculation process for the dielectric function is equivalent to searching for suitable matrix that minimizes the fitness function which denotes the degree of matching between the experimental and theoretical transmittance curves. The genetic algorithm in MATLAB software is used to seek better solution set, and the fitness values for all the retrieved dielectric functions are small than 0.05.

Square arrays of AZO nanodisks on silicon substrate with a period of 2 μm are fabricated to study their LSPR behaviors. For patterning nanodisk array, a polymethyl methacrylate (PMMA) layer is spin-coated on the cleaned Si substrate and patterned by electron-beam lithography. AZO film is sequentially deposited on the patterned PMMA film by RF magnetron sputtering. Then, a lift-off process is implemented to remove the patterned PMMA film with acetone and alcohol, and the sample is blown dry with N_2 gas. The sputtering and annealing conditions are the same as those of AZO films. The optical properties of AZO nanodisk arrays are obtained by Fourier transform infrared spectroscopy (FTIR) measurements. The experimental trends are verified with simulations using three-dimensional finite element method (3D FEM) by COMSOL Multiphysics software. The dielectric function of AZO nanodisk is adopted from that of AZO film retrieved by fitting methods as mentioned above, and the environmental refractive index is set as 1.0 for air. The scattering boundary condition for all the external boundaries of the computational domain is employed to

#255390 Received 10 Dec 2015; revised 17 Feb 2016; accepted 25 Feb 2016; published 1 Mar 2016

investigate the optical behavior without considering any optical couplings. Furthermore, the structural dimensions of nanodisks used in these simulations are identical to those of fabricated nanodisks.

3. Results and discussions

3.1. Plasmonic Properties of AZO Material

The electro-optical characteristics of AZO films can be easily tailored by adjusting deposition and annealing conditions since AZO material is a non-stoichiometric compound. Here, AZO films with thickness of 235 nm under different annealing temperatures and annealing atmospheres are fabricated to investigate their plasmonic behaviors. The electric properties of AZO films under different annealing temperatures (as-grown, 400, 500, and 600°C in N_2 for 1 hour) are obtained by Hall measurements. The results are listed in Table 1. All AZO films reveal the n-type property because of the natural defects (oxygen vacancies and zinc interstitials) and Al dopants in material [21]. The carrier concentrations of AZO films all reach 10^{20} cm^{-3} level, which implies that the metallic characteristic can be supported in the NIR region. By introducing an annealing process, the electric properties become better because the crystal quality of AZO film and substitution of Al in Zn lattice sites are improved, which results in enhanced carrier mobility, reduced resistivity, and increased carrier concentration [22]. A maximum carrier concentration is observed when the annealing temperature is 500°C.

Table 1. Electric properties of AZO films annealed at different temperatures.

Electric property	Annealing temperature			
	As-grown	400°C	500°C	600°C
Carrier concentration (#/cm^3)	1.60×10^{20}	3.95×10^{20}	4.56×10^{20}	4.26×10^{20}
Carrier mobility (cm^2/V-s)	4.93	5.40	9.48	12.26
Resistivity (Ω-cm)	7.92×10^{-3}	2.93×10^{-3}	1.44×10^{-3}	1.20×10^{-3}

The structural properties of AZO films under different annealing temperatures are examined by high-resolution X-ray diffraction (XRD) analysis, as shown in Fig. 1(a). For ZnO films, the peaks for (002), (101), and (102) appear at 2θ = 34.68°, 36.46°, and 47.50° [23]. For all Al-doped ZnO films, strong peaks are observed between 34.47° and 34.60°, but there are no obvious peaks around 36.46° and 47.50° (data not shown). This means that AZO films with the (002) diffraction peak possess hexagonal wurtzite structure and *c*-axis orientation to surface on the quartz substrate. The position of (002) peak slightly shifts to larger angle from 34.47° to 34.60° when raising the annealing temperature because of the variation of the residual stress in the film [24,25]. Average grain size in AZO film is determined from Scherer formula [26]. The calculated grain sizes of AZO films are 15.83, 15.93, 16.06, and 16.32 nm for as-grown and annealed samples at 400, 500, and 600°C.

The transmittance spectra of AZO films under different annealing temperatures are measured by a variable-angle UV/VIS/NIR spectrophotometer. The results are given in Fig. 1(b). All annealed films exhibit an average transmittance of 85% in the visible range. The squared absorption coefficients of AZO films as a function of photon energy are shown in Fig. 1(c), and the corresponding optical bandgaps obtained by Tauc's equation [27] are 3.43, 3.64, 3.71, and 3.69 eV for as-grown and annealed AZO films at 400, 500, and 600°C. From Burstein-Moss effect [28], the optical bandgap increases when there are more charge carriers in material. The results obtained here are consistent with those from Hall measurements and a maximum optical bandgap occurs when the annealing temperature is 500°C.

#255390 Received 10 Dec 2015; revised 17 Feb 2016; accepted 25 Feb 2016; published 1 Mar 2016

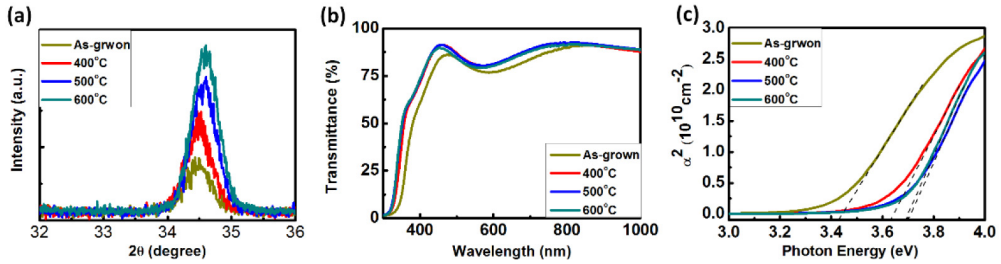

Fig. 1. (a) XRD analysis, spectra of (b) transmittance and (c) squared absorption coefficient of AZO films annealed at different temperatures.

Then, AZO films annealed in vacuum, N_2, air, and O_2 atmospheres at 500°C for 1 hour are fabricated, and their electrical properties are listed in Table 2. The carrier concentrations of AZO films drop far below 10^{20} cm^{-3} level when annealing in air and O_2 atmospheres, which indicates that the metallic properties cannot be supported in the NIR region. In fact, AZO films annealed in atmosphere with oxygen will result in considerable decrease in carrier concentration and mobility. First, oxygen will fill the oxygen vacancies in AZO film, causing the reduction in carrier concentration. Second, oxygen can be easily trapped at the grain boundaries to form Al–O bonds. As a result, some of Al ions become inactive, i.e., no free electrons are released. At the same time, such bonds could impede the motion of carriers, thereby degrading carrier mobility [29]. Besides, compared with the one annealed in vacuum, AZO film annealed in N_2 shows better electric properties because the inert gas, nitrogen, can diminish the defects such as dangling bonds at grain boundaries or film surfaces during the annealing process.

Table 2. Electric properties of AZO films annealed in different atmospheres.

Electric property	Annealing atmosphere			
	Vacuum	N_2	Air	O_2
Carrier concentration (#/cm^3)	2.14×10^{20}	4.56×10^{20}	1.32×10^{18}	2.51×10^{17}
Carrier mobility (cm^2/V-s)	5.37	9.48	2.42	1.74
Resistivity (Ω-cm)	5.43×10^{-3}	1.44×10^{-3}	6.35	14.30

The XRD measurements of AZO films annealed in different atmospheres are shown in Fig. 2(a). The peak values of 2θ are located at 34.58°, 34.52°, 34.68°, and 34.48° for AZO films annealed in vacuum, N_2, air, and O_2. This indicates that AZO films annealed in different atmospheres all have a *c*-axis orientation perpendicular to the surface of substrate. The corresponding calculated grain sizes are 16.31, 16.06, 17.02, and 16.56 nm. The transmittance spectra of AZO films annealed in different atmospheres are given in Fig. 2(b) and exhibit high average transmittance in the visible region. Figure 2(c) shows the squared absorption coefficient as a function of photon energy. The optical bandgaps of AZO films annealed in air and O_2 atmospheres are ~3.32 eV, close to that of ZnO film (3.30 eV), which implies that most Al dopants are inactive. On the other hand, for AZO films annealed in vacuum and N_2 atmospheres, the optical bandgaps are at higher values owing to the substantial free carriers provided by Al dopants.

#255390 Received 10 Dec 2015; revised 17 Feb 2016; accepted 25 Feb 2016; published 1 Mar 2016

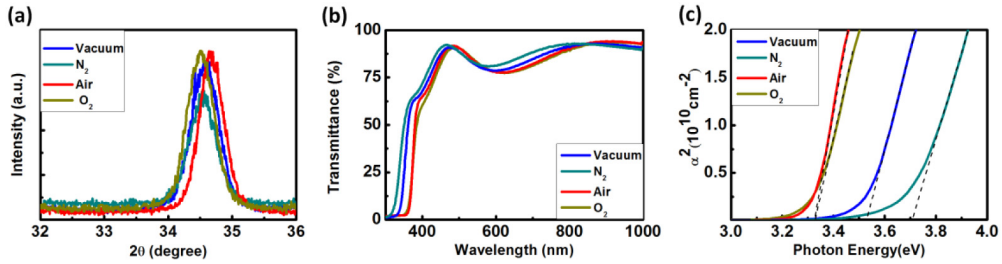

Fig. 2. (a) XRD analysis, spectra of (b) transmittance and (c) squared absorption coefficient of AZO films annealed in different atmospheres.

The dielectric function of AZO film in the range from 1500 to 4000 nm is retrieved by fitting a Drude-Lorentz oscillator model to the transmittance spectrum measured using FTIR. As shown in Fig. 3(a), the crossover wavelengths (where the real part, ε', of the dielectric function changes from negative to positive) for samples annealed in N_2 and vacuum are 1775 and 2397 nm, but no crossover are observed for samples annealed in O_2 and air. Since higher carrier concentration results in shorter crossover wavelength, our fitting results are consistent with Hall measurements. The imaginary part, ε'', of the dielectric function represents the optical loss in the material. From Fig. 3(b), ε'' for samples annealed in N_2 and vacuum are larger than those in O_2 and air. This is mainly because more free carriers lead to more free-carrier absorption. The optical properties of AZO films annealed in O_2 and air are just like those of dielectric material. Figures 3(c) and 3(d) shows the dielectric functions of AZO films annealed at different temperatures. The crossover wavelengths for the annealed samples are much shorter than the as-grown sample owing to the differences in the carrier concentration, as discussed previously. In Fig. 3(d), it is worthy to note that optical losses in AZO films are significantly lower compared with those in conventional metals such as gold and silver [30]. From these results, the metal-like and low-loss optical properties of AZO materials in the NIR region are successfully achieved and easily tuned through various annealing conditions.

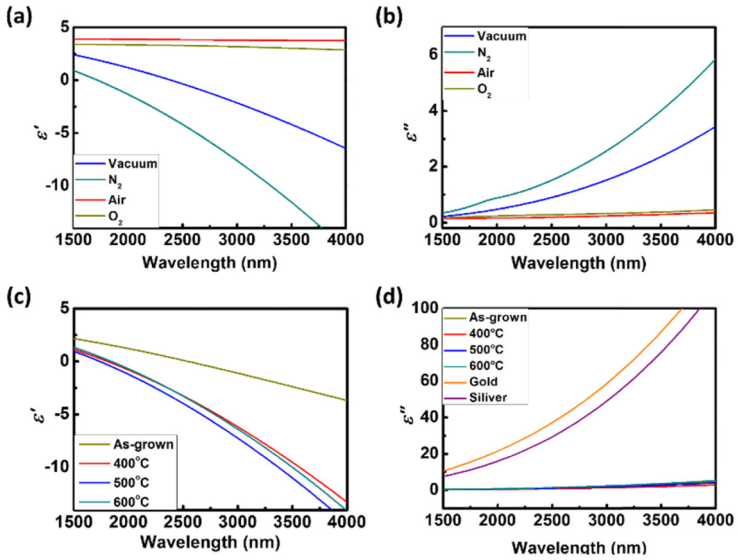

Fig. 3. (a) Real and (b) imaginary parts of the dielectric functions of AZO films under different annealing atmospheres. (c) Real and (d) imaginary parts of the dielectric functions of AZO films under different annealing temperatures.

#255390 Received 10 Dec 2015; revised 17 Feb 2016; accepted 25 Feb 2016; published 1 Mar 2016

AZO films annealed in N_2 at 500°C for 1 hour with different thicknesses are also fabricated by controlling sputtering duration. The measured electric properties are listed in Table 3 and small fluctuations are observed when varying the thickness of AZO film from 190 to 265 nm. XRD analyses of these films are given in Fig. 4(a). The corresponding diffraction peak positions remain at ~34.50° and the grain size is ranged from 16.06 to 16.55 nm. Figures 4(b) and 4(c) show the spectra of transmittance and squared absorption coefficient. Different oscillating fringes occur in the transmittance spectra because of interferences resulted from different thicknesses, and the optical bandgaps are all around 3.7 eV. From these results, we know that there are small variations on the structural, electric, and optical properties of AZO films with different thicknesses although the same annealing condition is applied. As a result, fluctuations in carrier concentrations and dielectric functions for samples with different thicknesses should be considered for the LSPR behavior of AZO nanodisk when altering thickness, which will be discussed in the following section.

Table 3. Electric properties of AZO films with different thicknesses.

Electric property	Film thickness			
	190 nm	215 nm	235 nm	265 nm
Carrier concentration (#/cm^3)	4.58×10^{20}	4.74×10^{20}	4.56×10^{20}	4.13×10^{20}
Carrier mobility (cm^2/V-s)	10.10	9.29	9.48	9.29
Resistivity (Ω-cm)	1.38×10^{-3}	1.42×10^{-3}	1.44×10^{-3}	1.63×10^{-3}

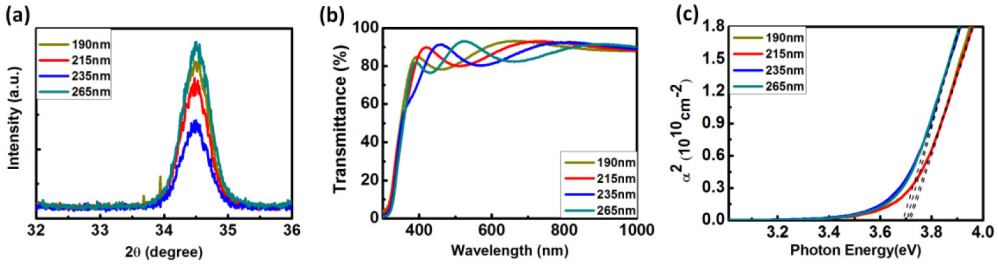

Fig. 4. (a) XRD analysis, spectra of (b) transmittance and (c) squared absorption coefficient of annealed AZO films with different thicknesses.

3.2. LSPR characteristics of AZO nanodisk arrays

A series of AZO nanodisk arrays under different annealing temperatures (as-grown, 400, 500, and 600°C in N_2 for 1 hour) and annealing atmospheres (vacuum, N_2, air, and O_2 at 500°C for 1 hour) are fabricated on silicon substrate to investigate the LSPR behaviors of TCO nanostructures. All nano-patterned arrays with the disk diameter of 740 nm and height of 235 nm are examined by scanning electron microscope (SEM) and atomic force microscope (AFM), as shown in Figs. 5(a) and 5(b). The nano-patterned array exhibits good uniformity within 300 × 300 μm^2 area. And there is no obvious change in the surface morphology and dimension of the nanodisk before and after the annealing process, as shown in Fig. 5(c). The measured and simulated extinction spectra of AZO nanodisk arrays under different annealing temperatures and annealing atmospheres are shown in Fig. 6. The resonance peaks are clearly observed and vary with different annealing temperatures because of the variation in carrier concentration. Higher carrier concentration means more metallic property, which results in blue-shift of the resonance peak. The resonance peak for the as-grown sample cannot be found for the wavelength range measured owing to the lower carrier concentration. The same trend is obtained for samples annealed in different atmospheres. Again, no peaks are found for samples annealed in air and O_2 owing to the much lower carrier concentrations. These results well agree with the electric and optical properties of AZO films obtained under different annealing conditions. The trends of simulated results also match with the experimental ones

#255390 Received 10 Dec 2015; revised 17 Feb 2016; accepted 25 Feb 2016; published 1 Mar 2016

when varying annealing temperatures and annealing atmospheres. The discrepancy of peak positions between simulated and experimental results may be attributed to three factors. First, the dielectric functions of the simulated and measured AZO nanodisks could be different. The former is adopted from AZO films deposited on quartz substrate, whereas the latter is from AZO nanodisks deposited on silicon substrate. Second, the shape of fabricated nanodisk, as shown in Fig. 5(b), is not the perfect disk shape employed in simulation. Third, there is a red-shift in resonance peak of the near-field spectrum of metallic nanostructure compared with that of the far-field spectrum [31,32]. Nevertheless, we demonstrate that LSPR behavior can be realized using metallic AZO nanodisk arrays.

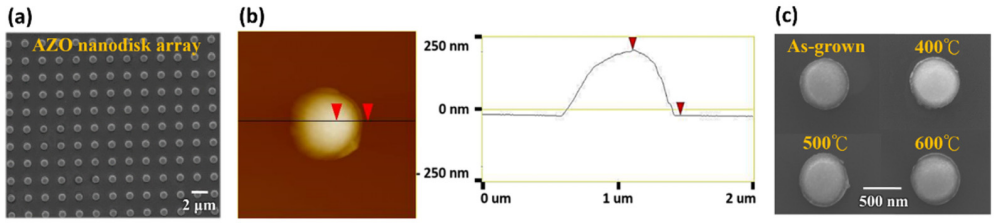

Fig. 5. Typical (a) SEM and (b) AFM images of AZO nanodisk array with diameter of 740 nm and height of 235 nm before annealing. (c) SEM images of AZO nanodisks after annealing at different temperatures.

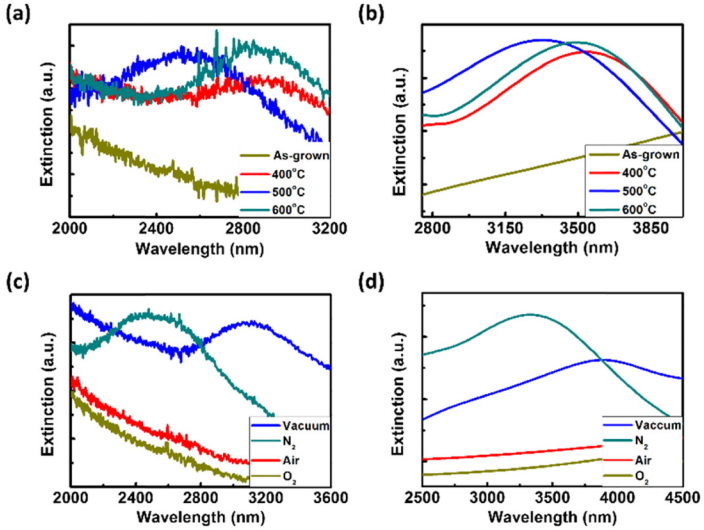

Fig. 6. (a) Measured and (b) simulated extinction spectra of AZO nanodisk arrays under different annealing temperatures (as-grown, 400, 500, and 600°C in N_2 for 1 hour). (c) Measured and (d) simulated extinction spectra of AZO nanodisk arrays under different annealing atmospheres (vacuum, N_2, air, and O_2 at 500°C for 1 hour).

Next, we study the influence of dimension of AZO nanodisk on the LSPR behavior. AZO nanodisk arrays with diameters varied from 600 to 950 nm annealed in N_2 at 500°C for 1 hour are prepared. The thickness is controlled at about 235 nm. Figure 7(a) shows the SEM images of fabricated AZO nanodisks with diameters of 600, 740, 840, and 950 nm. The measured and simulated extinction spectra of AZO nanodisk arrays with different diameters are shown in Figs. 7(b) and 7(c). The dielectric function retrieved from AZO film with thickness of 235 nm annealed in N_2 at 500°C for 1 hour is adopted in simulations. Clearly, the resonance peak of AZO nanodisk shifts to longer wavelength when enlarging the disk diameter in both experiment and simulation as expected owing to the reduced restoring force in the system

#255390 Received 10 Dec 2015; revised 17 Feb 2016; accepted 25 Feb 2016; published 1 Mar 2016

[32]. This LSPR peak is identified as a dipole mode from simulation analysis. The corresponding electric field intensity and surface charge distributions are shown in Figs. 8(a) and 8(b). Therefore, we show that the optical properties of nanodisks made of AZO materials are analog to those made of conventional metals.

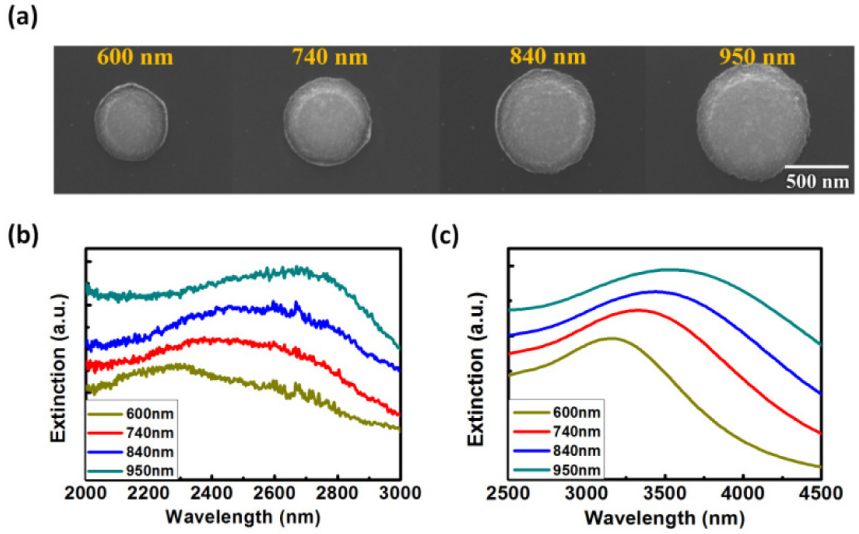

Fig. 7. (a) SEM images, (b) measured and (c) simulated extinction spectra of AZO nanodisk arrays with different diameters (600, 740, 840, and 950 nm) annealed in N_2 at 500°C for 1 hour.

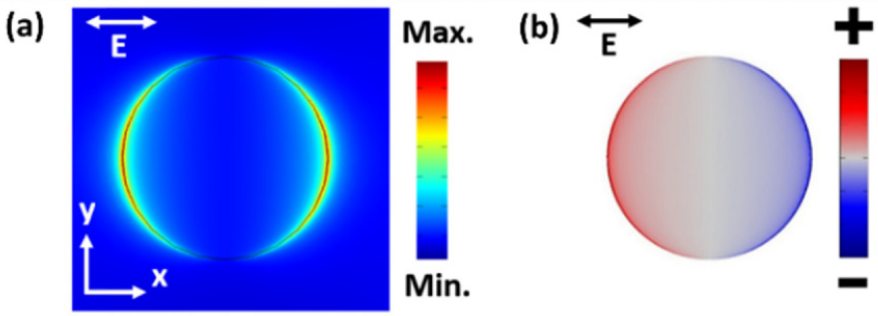

Fig. 8. Typical simulated (a) Electric field intensity and (b) surface charge distribution of AZO nanodisk with a thickness of 235 nm and diameter of 600 nm.

To examine the influence of thickness on the plasmonic behavior, AZO nanodisk arrays with thicknesses varied from 210 to 270 nm annealed in N_2 at 500°C for 1 hour are fabricated by controlling sputtering duration, while the diameter of AZO nanodisks is fixed at 600 nm, as shown in Fig. 9(a). Figures 9(b) and 9(c) show the corresponding measured and simulated extinction spectra of AZO nanodisk arrays with different thicknesses. The simulated spectra show slight blue-shift when increasing thickness as a result of increase of resorting force in the system [33]. The same dielectric function retrieved from AZO film with thickness of 235 nm annealed in N_2 at 500°C for 1 hour is adopted in simulations. However, as discussed above, though under the same annealing condition, there is fluctuation in carrier concentrations for samples with different thicknesses. Hence, LSPR peak shift is not obvious in experiments. In other words, the variations on restoring force and carrier concentration have to be considered for the LSPR behavior of AZO nanodisk when altering thickness.

#255390 Received 10 Dec 2015; revised 17 Feb 2016; accepted 25 Feb 2016; published 1 Mar 2016

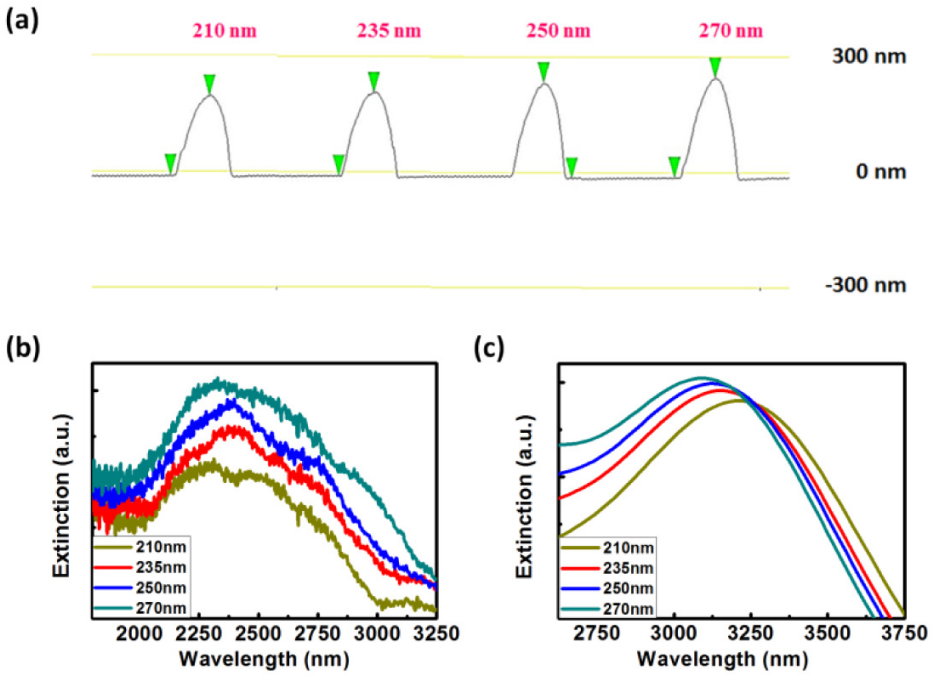

Fig. 9. (a) AFM plots, (b) measured and (c) simulated extinction spectra of AZO nanodisk arrays with different thicknesses (210, 235, 250, and 270 nm) annealed in N_2 at 500°C for 1 hour.

3.3. Capability of environmental index sensing using metallic AZO nanodisk array

To evaluate the capacity of environmental index sensing, the sensitivity of AZO nanodisk array is measured by immersing sample in index matching liquids with different refractive indices. The diameter and thickness of AZO nanodisk array are 600 nm and 235 nm. Figure 10(a) shows the measured extinction spectra after smoothing and normalization. The peak wavelength shifts from 2406 nm to 2718 nm when the refractive index is changed from 1.00 to 1.36. A high sensitivity of 873 nm/RIU is obtained by calculating the slope of the fitting curve via the least-square method, as shown in Fig. 10(b). The simulated extinction spectra are shown in Fig. 10(c). The peak wavelength shifts from 3160 nm to 3520 nm when the refractive index is varied from 1.00 to 1.36. The simulated sensitivity of AZO nanodisk is 1000 nm/RIU, as shown in Fig. 10(d). Hence, we demonstrate not only the metallic properties of AZO films and the LSPR characteristics of AZO nanostructures under various annealing conditions and structural dimensions, but also the environmental index sensing ability of AZO nanostructures. These results show the feasibility of using the metallic AZO material for plasmonic applications.

#255390 Received 10 Dec 2015; revised 17 Feb 2016; accepted 25 Feb 2016; published 1 Mar 2016

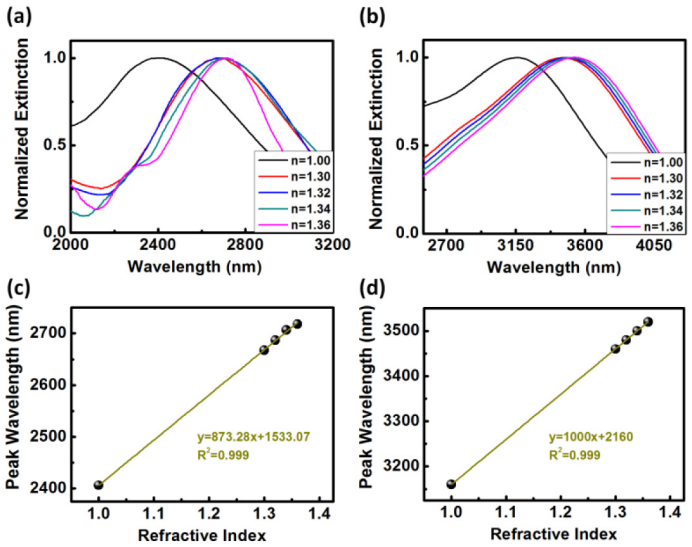

Fig. 10. (a) Measured and (b) simulated extinciton spectra of AZO nanodisk array when the environmental refarctive index is varied. (c) Measured and (d) simulated LSPR peak wavelength of AZO nanodisk array as a function of environmental refractive index.

4. Conclusion

The structural, electric, and optical properties of AZO films with various thicknesses deposited by RF magnetron sputtering under different annealing temperatures and annealing atmospheres are measured to investigate their metallic characteristics. It is found that AZO can possess features of metal-like, low optical loss, and highly tunable plasmonic resonance in the NIR region under proper annealing conditions, which are beneficial for plasmonic applications. Meanwhile, the dielectric functions of AZO films are retrieved by fitting a Drude-Lorentz oscillator model to the transmittance spectra and then employed in simulations to carry out the predicted optical behaviors of AZO nanostructures. Metallic AZO nanodisk arrays with various diameters and thicknesses under different annealing temperatures and annealing atmospheres are fabricated to explore their LSPR behaviors. Clear LSPR peaks are observed and highly depend on the annealing condition and structural dimension in both experiment and simulation. Thus, our results show that AZO nanostructure is promising to serve as a new plasmonic nanostructure with highly tunable and low-loss properties. To demonstrate its capability as a building block for plasmonic applications, we apply AZO nanodisk array for optical index sensing. High sensitivity of 873 nm/RIU in experiment is obtained. Taking with the advantages of excellent sensing ability on gas or biochemistry using AZO material, we believe that highly sensitive and responsive optical nano-sensor can be expected in the future.

Acknowledgments

This work is supported by Taiwan's Ministry of Science and Technology (MOST) under contract number MOST 103-2221-E-009-096-MY3. The authors would like to thank the equipment support from Center for Nano Science and Technology (CNST) and Nano Facility Center (NFC) at National Chiao Tung University (NCTU), Taiwan. We would like to acknowledge Dr. Min-Hsiung Shih for the support of FTIR measurements at Research Center for Applied Sciences, Academia Sinica.

#255390 Received 10 Dec 2015; revised 17 Feb 2016; accepted 25 Feb 2016; published 1 Mar 2016